February 15, 1994

Line-of-Sight Tropospheric Calibration From Measurements in Arbitrary Directions

J. Z. Wilcox

Tracking Systems and Applications Section

Tropospheric inhomogeneities limit the accuracy with which a path delay in an arbitrary direction can be estimated from calibration measurements in different directions. This article demonstrates a mathematical procedure that has the potential for minimizing errors in the estimated geometrical and tropospheric path delays. The error is minimized by applying least-squares estimation to a combined set of observables in the calibration directions and the direction to be calibrated. A simulated test of this procedure was conducted using a model set of error-free calibration measurements. In the absence of geometrical delay mismodeling, the simulation yielded delay errors which vary from about 1 mm at zenith to about 1 cm at 10 deg. The main principles of how this procedure could be applied to improve accuracy of deep space tracking using Global Positioning System (GPS) data are also discussed.

I. Introduction

Uncertainties in tropospheric path delays are a major source of error in deep space tracking. Inhomogeneities in tropospheric water vapor can result in zenith path delay calibration errors at about the 1-cm level, and inhomogeneities in the dry troposphere at about the 1- to 3-mm level, over a period of several hours [1]. The 1-cm error limits the tracking accuracy of DSN-based very long baseline interferometry (VLBI) to about 1 nrad for the angular position (at the intercontinental baselines of about 10,000 km) and to 2×10^{-14} sec/sec for the delay rate (at zenith) for a 1000-sec scan [1]. Future missions would benefit from troposphere calibration at the 1-mm level.

The error in the estimated path delay is determined by a variety of error sources whose relative importance depends on the calibration instrument. For example, for instruments which measure radio emission, such as water vapor radiometers (WVRs), the error is limited by the accuracy with which path integrals involving the imaginary part of the index of refraction can be related to integrals which involve the real part of the refraction index [2]. Whereas WVRs may be pointed in the direction to be calibrated, this may not be true in general for other instruments. If off-line-of-sight measurements are used in the calibration process, the error will inevitably be affected by tropospheric inhomogeneities, and its magnitude will depend on mathematical analysis of calibration data.

This article suggests and illustrates a mathematical procedure that minimizes the tropospheric inhomogeneity-induced error for path delays inferred from observables in other directions. The procedure involves the application of least-squares estimation to a combined set of observables in the calibration directions and the direction to be cali-
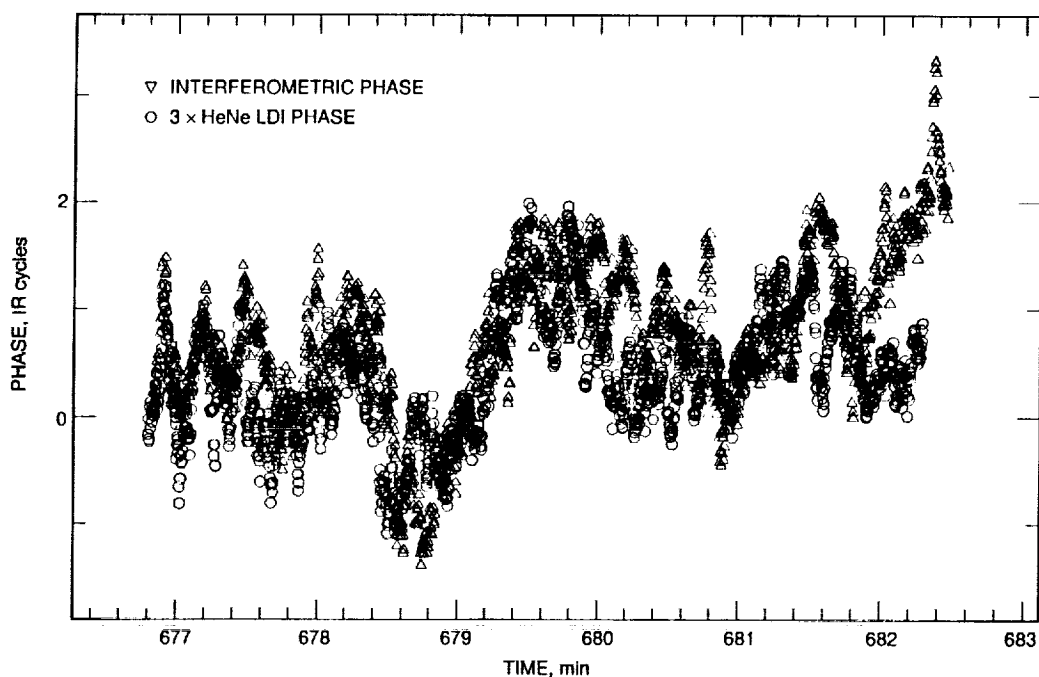
Fig. 5. The phase time series of Fig. 3 with HeNe LDI phases, scaled to infrared cycles, differenced between telescopes, and multiplied by 3.
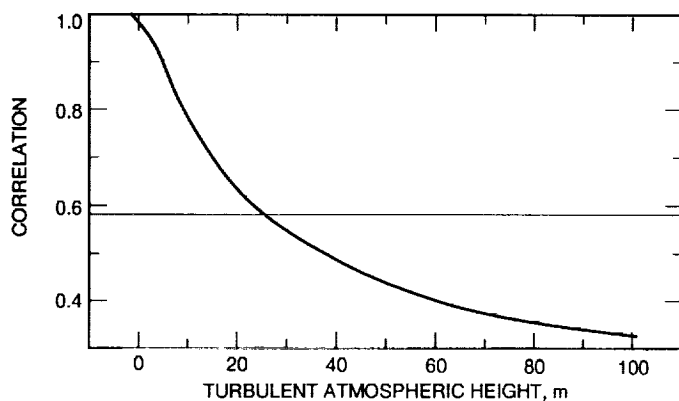

Fig. 6. The calculated correlation between telescope-differenced HeNe LDI data and interferometric data for the conditions of the data in Figs. 3–5. The horizontal line is the actual correlation from the data of Fig. 5.
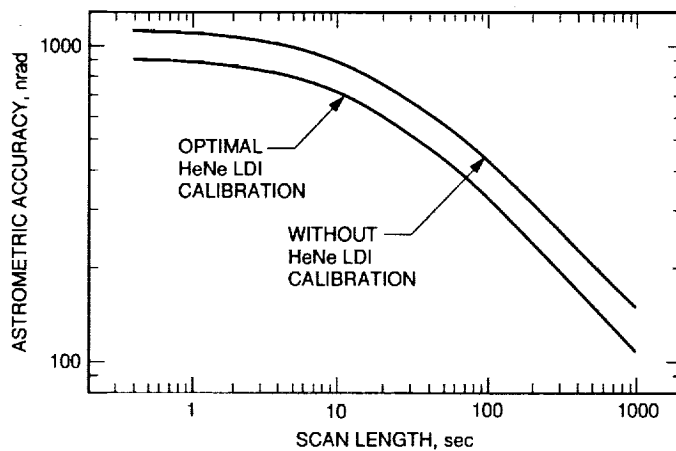
Fig. 7. The calculated astrometric accuracy, as a function of scan length, with and without optimal HeNe LDI calibration, for the conditions of Figs. 3–5.

brated, and the use of the observable variance–covariance matrix during estimation. In order to demonstrate the procedure simply, this article makes the following assumptions: The calibration instrument is error-free (i.e., no other error source besides tropospheric inhomogeneities is present), and it detects path delays. These assumptions are used for clarity of the presentation; the method may be generalized to other types of measurements. An example of how it can be adopted to more realistic (noisy) data is discussed in Section IV of this article. If all other error sources are neglected, the calculated error determines the maximum achievable accuracy for path delay estimates using observables in other directions. Another (more commonly used) procedure determines the delay in the zenith direction by averaging over delays projected into the zenith from many calibration directions. This technique will be referred to in this article as "zenith mapping." Strictly speaking, zenith mapping produces minimal error only for a horizontally homogeneous troposphere. This article will quantify the error reduction obtained from the use of the present technique for an inhomogeneous troposphere. Since the technique's principal intended application is to improve the accuracy of deep space tracking, the direction to be calibrated will be sometimes referred to in this article as the DSN antenna pointing direction.

Section II describes the mathematical procedure used to minimize the estimated delay error. The procedure is exemplified in Section III for a model set of calibration directions (assuming error-free instrumentation) that coincides with directions of lines between a ground-based receiver and Global Positioning System (GPS) satellites visible at Goldstone.[1] These directions were selected as a matter of convenience and because they are known with great accuracy.[2] Tropospheric inhomogeneities were assumed to be generated by Kolmogorov turbulence and transported past the observer by the wind [1]. Section IV discusses the possibility of adapting the procedure to GPS data. Section V is a summary with recommendations for further studies.

II. Mathematical Approach

This section outlines the main principles of the mathematical procedure that minimizes the estimated delay er-

ror in an arbitrary direction. The main principle of the procedure is the application of least-squares estimation to a combined set of observables in the calibration directions and the direction to be calibrated (also referred to as the pointing direction of the DSN antenna), and the use of the covariance–variance matrix of observables to weight the quadratic form of observable residuals during estimation. To simplify the illustration, all measurements are assumed to be error-free and to have produced path delays.

The coordinate system is shown in Fig. 1. A calibration instrument, located at the distance $\vec{R}$ from the axis of the DSN antenna, measures tropospheric path delays $L_{tr,i}$ in N different directions (E_i, ϕ_i), where E_i and ϕ_i are elevations and azimuths, respectively, and $i = 1, ..., N$. A DSN antenna (the direction to be calibrated) points in the direction of the elevation, E_s, and azimuth, ϕ_s. By assuming that the ionospheric delay has been calibrated (e.g., by using two frequency measurements), the DSN antenna-measured delay is $L_{tot,s} = L_{g,s} + L_{tr,s}$, where $L_{tot,s}$, $L_{g,s}$, and $L_{tr,s}$ are the total, geometric, and tropospheric delays, respectively. The combined set of observables in the DSN antenna and calibration directions is:

$$L_{tot,s} = L_{tr,s} + L_{g,s} \qquad (1a)$$

$$L_i = L_{tr,i} \quad i = 1, ..., N \qquad (1b)$$

where the symbol L_i designates the observable $L_{tr,i}$. The delay of interest for deep space tracking is the geometrical delay $L_{g,s}$. To obtain the best estimate $\hat{L}_{g,s}$, we (1) note that $L_{tr,s}$ and $L_{tr,i}$'s are related through tropospheric correlations, (2) parameterize Eqs. (1a) and (1b) with the help of the statistically averaged zenith delay $L_{tr,z}$ (that is, $L_{tr,z}$ is not the instantaneous zenith delay, but rather a delay averaged over all possible tropospheric patterns for the site [1]), and (3) apply least-squares estimation to the parameterized Eqs. (1a) and (1b). Assuming that long-range refraction gradients [6] are absent,[3] the parameterized $L_{tr,s} = \langle L_{tr,s} \rangle + \epsilon_{tr,s}$ and $L_{tr,i} = \langle L_{tr,i} \rangle + \epsilon_{tr,i}$, where $\langle L_{tr,s} \rangle = A_s L_{tr,z}$ and $\langle L_{tr,i} \rangle = A_i L_{tr,z}$, $\langle ... \rangle$ designates the expectation value, A_s and A_i are air masses, and $\epsilon_{tr,s}$ and $\epsilon_{tr,i}$ represent tropospheric inhomogeneities in (E_s, ϕ_s) and (E_i, ϕ_i) directions, respectively. Note that because of (2) above, correlations of $\epsilon_{tr,s}$ and $\epsilon_{tr,i}$ can be evaluated in the statistical sense. By defining the observable, parameter, and tropospheric inhomogeneity column vectors $F \equiv [L_{tot,s}/A_s, L_i/A_i]$, $X \equiv [L_{tr,z}, L_{g,s}/A_s]$,

---

[2] Other off-line-of-sight measurements to which the method may be adapted include microwave temperature profiler [3], lidar [4], radio acoustic sounding [5], and tracking using a number of proposed communication satellites systems, such as Motorola's IRIDIUM constellation.

[3] Unmodeled horizontal gradients may be on the 1-cm level for dry delays at 10-deg elevation [6]; the error can be reduced by gradient modeling during estimation.

and $\epsilon \equiv [\epsilon_{tr,s}, \ \epsilon_{tr,i}]$, respectively, and by assuming that $\epsilon_{tr,i}$'s have zero means and a variance–covariance matrix W^{-1}, the parametrized Eqs. (1a) and (1b) are solved by minimizing the quadratic form of the weighted residuals $(F - \mathcal{A}\hat{X})^T \ W \ (F - \mathcal{A}\hat{X})$, where $\mathcal{A}$ is the mapping matrix in $F = \mathcal{A} \ X + \epsilon$,

$$\mathcal{A} = \begin{pmatrix} 1 & 1 \\ 1 & 0 \\ \vdots & \vdots \\ 1 & 0 \end{pmatrix} \tag{2}$$

The result is [7]

$$\hat{X} = (\mathcal{A}^T W \mathcal{A})^{-1} \mathcal{A}^T W \ F \tag{3}$$

where $\hat{X}$ is the column vector $\hat{X} \equiv [\hat{L}_{tr,z}, \ \hat{L}_{g,s}/A_s]$, and the superscript T designates the transpose matrix. The error in $\hat{L}_{g,s}$ is given by the square root of the matrix element $(\sigma_{\hat{X}}^2)_{2,2}$ of the variance $\sigma_{\hat{X}}^2$:

$$\sigma_{\hat{X}}^2 \equiv \left\langle (\hat{X} - X)(\hat{X} - X)^T \right\rangle$$

$$= B^{-1} \mathcal{A}^T W \ \text{cov}\,(F, F^T) \ W \ \mathcal{A} \ B^{-1} \tag{4}$$

where cov (F, F^T) is the observable covariance–variance matrix, and $B \equiv \mathcal{A}^T \ W \ \mathcal{A}$.

The above-described procedure yields the best estimate $\hat{L}_{g,s}$ and $\hat{L}_{tr,z}$. Note, however, that once $\hat{L}_{g,s}$ has been estimated, Eq. (1a) can also be used to estimate the actual line-of-sight tropospheric delay $L_{tr,s}$. By using Eq. (1a), the estimate $\hat{L}_{tr,s} \equiv L_{tot,s} - \hat{L}_{g,s}$. $\hat{L}_{tr,s}$ is the best estimate for $L_{tr,s}$ because $\hat{L}_{g,s}$ is the best estimate for $L_{g,s}$, and because the measured $L_{tot,s}$ contains the effect of line-of-sight inhomogeneities (note that $\hat{L}_{tr,s}$ differs from $\hat{L}_{tr,z} A_s$, which is the best estimate for the statistically averaged delay). Note also that in the absence of other error sources, the error in $\hat{L}_{tr,s}$ is equal to the error in $\hat{L}_{g,s}$.

It will be useful for the ensuing discussion to explicitly write $\hat{L}_{tr,s}$ as[4]

$$\hat{L}_{tr,s} \equiv L_{tot,s} - \hat{L}_{g,s} = L_{tot,s} - A_s \hat{X}_2 = \sum_{i=1}^{N} c_i L_{tr,i} \tag{5}$$

where $c_i \equiv -(A_s/A_i) \ ((\mathcal{A}^T W \mathcal{A})^{-1} \mathcal{A}^T W)_{2,i+1}$ represents contributions from the ith calibration direction. By using Eq. (5), the estimated delay error can be expressed as follows:

$$\sigma_{L,tr,s}^2 = \sigma_{L,g,s}^2 = \left\langle \left(L_{tr,s} - \sum_{i=1}^{N} c_i L_{tr,i} \right)^2 \right\rangle$$

$$= \left\langle L_{tr,s}^2 \right\rangle - 2 \sum_{i=1}^{N} c_i \left\langle L_{tr,s} \ L_{tr,i} \right\rangle$$

$$+ \sum_{i,j=1}^{N} c_i c_j \left\langle L_{tr,i} \ L_{tr,j} \right\rangle \tag{6}$$

Equation (6) displays an explicit dependence on the coefficients c_i's and on correlations between tropospheric path delays. When c_i's are determined by using some assumed W^{-1} (the so-called consider analysis [1]), the error will be bigger than the error obtained by using the actual observable W^{-1} [7]. A W^{-1} often used during the estimation procedure is the diagonal matrix, $W_{i,j}^{-1} = \delta_{i,j}$ (where $\delta_{i,j}$ is the Kronecker delta). The use of a diagonal W^{-1} corresponds to assuming that observable errors are uncorrelated, and Eq. (3) yields[5] $c_i = A_s/(NA_i)$, which are the same c_i's as those which would be obtained if one set $\hat{L}_{tr,z} \equiv \sum_{i=1}^{N} L_{tr,i}/(A_i \ N)$, and mapped $\hat{L}_{tr,z}$ from the zenith to the (E_s, ϕ_s) direction by using the air mass A_s. The use of zenith mapping will minimize the error only for a horizontally homogeneous troposphere. For an inhomogeneous troposphere, the error is minimized by using the observable $W^{-1} = \text{cov}\,(F, F^T)$; c_i's will then depend on the full (in elevation and azimuth) angular separations between the observed and calibration directions (including the offset $\vec{R}$). By setting $W^{-1} = \text{cov}\,(F, F^T)$, Eq. (4) reduces to $\sigma_{\hat{X}}^2 = (\mathcal{A}^T W \ \mathcal{A})^{-1}$

III. Results for an Error-Free Calibration Instrument

Equation (6) was evaluated for a model set of calibration directions assumed to coincide with directions of lines between a ground-based receiver and GPS satellites visible at Goldstone. These directions were selected because there are between 6 and 10 satellites visible from any ground-based site, and the satellite trajectories are known with

---

[4] The proportionality coefficient between $\hat{L}_{g,s}$ and $L_{tot,s}$ is equal to 1 because no other observable depends on $L_{g,s}$.

[5] For elevation-independent correlations, $W_{i,j}^{-1} = \delta_{i,j}/A_i A_j$, the coefficients would become $c_i = A_s A_i / \sum_{i=1}^{N} A_i^2$.

great accuracy. Other directions could be selected; conclusions similar to those derived here will apply to all other selections. The error was quantified by using the Kolmogorov turbulence model for the evaluation of correlations between wet troposphere inhomogeneities, with numerical constants given in [1] (see also Appendix A of this article). The inhomogeneities were frozen into the troposphere slab transported past the observer with the wind velocity $\vec{v} = 10$ m/sec. The structure function constant $C = 1.1 \times 10^{-7} m^{-1/3}$ corresponds to average DSN observation conditions of about a 6-cm zenith wet delay for $h_v = 2$-km-thick wet troposphere slab [8]; in more humid weather, the structure constant will be greater, depending on turbulence. The dry fluctuation was assumed to be 30 percent of the wet fluctuation [1], which for uncorrelated fluctuations contributes less than 10 percent of the total error for correlations added in quadrature. The error evaluated with the optimized c_i's was compared to the zenith mapping error; the zenith mapping error was greater, especially at low elevations, as expected. The error was quantified for a number of directions (E_s, ϕ_s), for satellite constellations stepped by 6 min during an 8-hr period following 12:00 a.m., July 23, 1992, and for four values of the separation $R = 0, 200, 500,$ and 1000 m. The biggest contribution to the estimated delay comes from a calibration direction nearest to the direction to be calibrated; the error vanishes when the two lines coincide. In the absence of a clearly nearest direction, all calibration lines contribute, increasing the error.

A. Delay Error

The error was found to depend in a relatively well-defined manner on the elevation E_s, but not (because the satellites are distributed over the azimuth fairly uniformly) on ϕ_s nor on satellite constellation. Figures 2(a) and 2(b) plot the azimuthally averaged error (dashed line) versus E_s for $R = 0$ and 1000 m. The error spread due to (1) a 360-deg range in ϕ_s, (2) a 360-deg range in the azimuth of $\vec{R}$, and (3) changes in the satellite constellation is also shown. The spread's lower bound is 0 for all E_s in Fig. 2(a) (E_s extends from 10 deg in Fig. 2(a) because the satellites were cut off at 10 deg). The bound is 0 because at $R = 0$, any direction E_s will, for some combination of ϕ_s and satellite constellation, eventually coincide with one of the calibration lines, in which event the tropospheric inhomogeneity-induced error vanishes. Note that the average error is closer to the error upper bound than to the lower bound, indicating that the error is nearly equal to the error upper bound in the majority of observations. Comparing Figs. 2(a) and 2(b), the average error has increased only very little, while the lower bound has become nonzero by increasing R from 0 to 1 km. The average

error has increased little because the DSN-observed and calibration lines intersect (and thus probe the same sky region) even when $R = 1$ km; the lower bound has become nonzero because there are no coincident lines when $R > 0$. The average error is fairly flat (about 1 mm) for all E_s between zenith and 40 deg, and it increases rapidly with decreasing E_s at lower elevations; the error is about 1.6 and 12 mm at $E_s = 30$ and 10 deg, respectively.

Figure 3 illustrates how close the calibration and DSN line must be for the error to be less than some desired value. The error (the solid-line curve) will be less than 0.5 mm when the angular separation between the DSN and the nearest calibration line ($R = 0$ in Fig. 3) is less than 3 deg. How small the angular separation must be depends on elevation: modeling results suggest that for the error to be less than 1 mm, the separation must be less than 5 and 2 deg when $E_s = 30$ and 20 deg, respectively. Many estimation strategies estimate zenith delays by averaging over all calibration directions. The zenith mapping error (the dash–dot line) is bigger than the optimized, azimuthally averaged error (the dashed line) by an amount which decreases monotonically with increasing elevation, until, near zenith, the errors are nearly the same (because the mapping distance is short there).

Signal integration averages out the tropospheric inhomogeneity-induced error as the inhomogeneities are carried by wind. Figure 4 shows the effect of the signal integration time T and wind velocity v on the error.[6] The error decreases and its spread (due to different wind directions) increases slowly with increasing T. Note that the average integration time, $T_{1/2}$, required to reduce the error to one-half of its instantaneous value is (for $v = 10$ m/sec) less than 8 min for all $E_s > 30$ deg, and it increases to about 12 min at $E_s = 10$ deg. To minimize the error, c_i's used for Fig. 4 were optimized for the wind. A similar calculation using c_i's optimized for zero wind has produced curves (not shown) that look the same as those in Fig. 4 except that the error was approximately 10 to 30 percent higher (depending on elevation). This relatively small increase is good news, since the determination and inclusion of wind distribution in the estimation procedure could be nontrivial.

The use of more than one calibration instrument will (in principle) increase the probability that one calibration line will be close to the observed line. Figure 5 shows the minimum error for three instruments positioned in corners

---

[6] $R = 200$ m is used in most figures in this article, since the azimuthally averaged errors do not differ too much for all R's $<$ 1 km, and since mounting a calibration instrument in the center of the DSN antenna is nontrivial.

of an equilateral triangle around the DSN antenna. Compared to one instrument (positioned at $R = 0$ and 200 m), the error is smaller by up to 50 percent at high elevations (where it is already small), but only by several percent at low elevations (where it would be needed the most because the error is big there). The result suggests that multiple on-site instruments will be of limited use.

B. Delay Rate Error

Figures 6 and 7 show the inhomogeneity-induced delay rate error. Rate measurements are used for navigation and gravitational wave searches; it is desirable that the inhomogeneity-induced rate error not dominate the total error on any time scale. The rate error was evaluated as the square root of the variance $\sigma_{\dot{B}}^2(T_{sc})$,

$$\sigma_{\dot{B}}^2(T_{sc}) \equiv \left\langle \left(\dot{B}(T_{sc}) - \hat{\dot{B}}(T_{sc}) \right)^2 \right\rangle \qquad (7)$$

where $\hat{\dot{B}}(T_{sc})$ and $\dot{B}(T_{sc})$ are the estimated and actual delay rates, respectively, over the scan duration T_{sc} (see [1] and Appendix B). The variance was evaluated by using a linear fit to three equally spaced points[7] within T_{sc}. Figure 6 shows the error evaluated by using the optimized c_i's, and compares it with the uncalibrated error and the error evaluated by using zenith mapping for two elevations, $E_s = 10$ and 60 deg. All three errors decrease with increasing T_{sc} (as they should). However, whereas the optimized error is actually slightly bigger than the uncalibrated and zenith mapping errors for extremely short scans ($T_{sc} < 10$ sec), the optimized error decreases with increasing T_{sc} more rapidly than the other errors, becoming smaller at a T_{sc} that depends on E_s. For example, at $E_s = 10$ and 60 deg, the error becomes smaller at $T_{sc} = 500$ and 30 sec, respectively. For the error to be reduced by using the optimized c_i's, the scan must be longer than some critical T_{sc}, which is longer at low E_s than at high E_s. At $T_{sc} = 1000$ sec ($R = 200$ m), the average error is about 4×10^{-15} sec/sec and 7×10^{-14} sec/sec at $E_s = 60$ and 10 deg, respectively.

The rate error can also become very small when the angular separation between the observed and nearest calibration line is sufficiently small; however, the condition for the separation smallness is tighter than that for the delay error. This is illustrated in Fig. 7 for $R = 0$. For the error to be less than 10^{-15} sec/sec, the angular separation must be less than about 0.5 deg when $T_s = 1000$ sec and less than about 0.05 deg when $T_s = 100$ sec.

---

[7] It can be shown that as the number of fitted points increases to infinity, the rate error changes by only about 20 percent [1].

IV. Application to GPS

This section discusses how the mathematical procedure described in Section III could be adapted to path delay estimation using GPS data. GPS tracking depends directly on path delays.[8] However, because of the complexities of GPS delay modeling and data reduction, the present approach to GPS data analyses, driven by the requirement to eliminate or estimate clock errors and geometrical parameter uncertainties,[9] entails estimation of instantaneous zenith delays [9]. Parameter estimation is performed without the use of the tropospheric covariance–variance matrix. The zenith tropospheric delay is constructed by spatial averaging over all satellites. This zenith delay could be used to estimate tropospheric delays in the direction of the DSN antenna by scaling it (using the air mass) into the DSN antenna direction. This article suggests that in the absence of other error sources, line-of-sight delays could be estimated more accurately by modifying the estimation strategy to include the tropospheric correlations between different lines of sight and by applying the estimation procedure to the combined GPS and DSN data.

The coordinate system is the same as in Fig. 1 except that receivers (which are a part of a large global network consisting of about 40 continuously operating receivers set up to estimate the geometrical parameters and to determine the clock uncertainties with the best possible accuracy) are separated by large (several hundred-km) distances. For M receivers, one can introduce M statistically averaged, mutually uncorrelated zenith delays, $L_{tr,j,z}$, where $j = 1, ..., M$. The DSN antenna is assumed to be at the site $j = 1$. At its completion, the GPS constellation will include 24 navigation satellites at about a 20,000-km altitude and equally spaced in six orbit planes. A receiver at any ground-based site will track between 6 and 10 satellites distributed more or less uniformly in azimuth and typically above 10 deg in elevation. The collected data set covers a time period long enough for the number of data in the set to exceed the number of solve-for parameters. Including the delay for the radio signal received by the DSN antenna, the observables are

$$L_{tot,s} = L_{tr,s} + L_{g,s} \qquad (8a)$$

---

[8] GPS receivers are used in an automated operating mode, work in all weather conditions, and sense the total (wet and dry) path delays. The satellites transmit carrier signals at two L-band frequencies (1.227 GHZ and 1.575 GHz), so that the ionospheric delay can be calibrated.

[9] S. M. Lichten, personal communication, Tracking Systems and Applications Section, Jet Propulsion Laboratory, Pasadena, California, October 1992.

$$L_{tot,i,j} = L_{tr,i,j} + L_{g,i,j} + L_{cl,i,j}$$

$$i = 1, ..., N \quad j = 1, .., M \tag{8b}$$

where N is the total number (assumed to be the same for all receivers) of calibration data at one receiver site (the subindex i counts both the visible satellites and the data sequence for each satellite), and $L_{cl,i,j}$ is a delay caused by clock estimate errors at both the satellite and the receiver. All other symbols are the same as in Section II, and the ionospheric delays have been assumed to be calibrated. Similar to Eqs. (1a) and (1b), Eqs. (8a) and (8b) can be parameterized by setting $\langle L_{tr,s} \rangle = A_s L_{tr,1,z}$ and $\langle L_{tr,i,j} \rangle = A_i L_{tr,j,z}$, where $L_{tr,j,z}$ are the statistically averaged tropospheric delays in the zenith direction at jth site. By assuming that the observable errors have zero means and a variance–covariance matrix W^{-1}, the parameterized Eqs. (8a) and (8b) can be solved by least-squares estimation for the geometrical delays $L_{g,s}$ and $L_{g,i,j}$ (or rather, by using geometrical delay modeling for parameters which determine $L_{g,s}$ and $L_{g,i,j}$), clock errors $L_{cl,i,j}$, and zenith delays $L_{tr,j,z}$. As was discussed in Section II, it is this parameterization, accompanied by the statistical evaluation of W^{-1}, that allows the solution to produce best estimates. Note also that once $L_{g,s}$ has been estimated, the best estimate for line-of-sight $L_{tr,s}$ can in principle be obtained as the difference $\hat{L}_{tr,s} = L_{tot,s} - \hat{L}_{g,s}$.

For real data, the accuracy of path delay estimates, in addition to tropospheric inhomogeneities, will be affected by other error sources, including instrument and multipathing noise and uncertainties in geometrical delay modeling. Neglecting the specifics of geometrical delay modeling and error statistics, the effect of an overall uncertainty level contributed by various error sources has been modeled by adding to each cov $(L_{tr,i}, L_{tr,i})$ a term assumed to be uncorrelated between different directions and proportional to the air mass. Figure 8 shows the effect of the assumed 0.1-, 0.3-, and 1-cm uncertainty levels.[10] Note that these levels exceed the tropospheric inhomogeneity-induced errors at $E_s = 50$, 22, and 12 deg, respectively. That is, to achieve the tropospheric inhomogeneity-limited accuracy at some elevation, the additional uncertainty must be reduced below the inhomogeneity-induced error at that elevation. The dashed curves in Fig. 8 show the error resulting from the use of c_i's which were optimized for zero measurement and modeling uncertainty. The errors are bigger than for the optimized c_i's by about 15 percent,

which is sufficiently small to argue that the use of c_i's optimized for zero additional uncertainty will not significantly increase the total error.

V. Conclusions and Recommendations

This article has outlined a mathematical procedure which has the potential for minimizing the tropospheric inhomogeneity-induced mapping error for estimated path delays along arbitrary lines of sight by using observables from different directions. The main principle of the procedure is the application of least-squares estimation to the combined set of observables in the calibration directions and the direction to be calibrated, and the use of an observable variance–covariance matrix during estimation. A numerical example was given for a set of calibration directions assumed to coincide with directions from a ground-based receiver to GPS satellites visible at Goldstone. For these directions, assuming an error-free calibration instrument and zero geometrical delay mismodeling, and using the Kolmogorov turbulence model, the azimuthally averaged error is found to be about 1 mm in the elevation range from about 40 deg to zenith. At elevations less than 40 deg, the error increases with decreasing elevation, reaching about 1.2 cm at 10 deg. Because of its stochastic origin, the inhomogeneity-induced error cannot be removed by improved modeling or instrument design, and represents the ultimate accuracy for line-of-sight estimates.

The minimum error was compared to the error obtained by using zenith delays which were averaged over many calibration directions, and to error obtained by using line-of-sight estimates optimized for zero wind. The zenith mapping error is nearly twice as large (in the absence of other error sources) as the minimum error, indicating that the effort spent to minimize the error is worthwhile. On the other hand, the error increase resulting from the use of zero wind was less than 30 percent, indicating that it may not be necessary to include the wind in the estimation procedure. Signal integration reduces the error; the integration time required to halve the instantaneous error is less than 8 min for elevations between 30 deg and zenith, reaching about 12 min at 10 deg. The use of multiple on-site receivers will not help to reduce the error at low elevations where it would be needed the most.

The suggested procedure could be used to estimate path delays in the direction of the DSN antenna by using GPS data. The present strategy for GPS data analyses entails construction of a tropospheric zenith delay by averaging over all satellites; the estimated zenith delay error is at the 1-cm level due to the combined effect of tropo-

---

[10] Analysis of recent GPS data shows that assumption of uncorrelated errors is not entirely correct. Efforts to understand the error statistics are under way.

spheric inhomogeneities, uncertainties in geometrical delay modeling, and measurement (thermal noise and multipathing) uncertainties [9]. The combined effect of additional uncertainties has been modeled by adding to the tropospheric variances a term assumed to be uncorrelated between various measurements. As expected, the accuracy of the estimate was limited by this additional term whenever it exceeded the tropospheric inhomogeneity-induced level. Further work should be performed to establish levels and statistics of additional error sources, incorporate their correlations into the analysis, and, if possible, reduce their effect on path delay estimates.

In spacecraft tracking, observing epochs and scan lengths are specified by mission considerations, and the tracked directions differ from satellite directions. However, experiments could be designed in which the direction to be calibrated coincides with one of the satellite directions. For example, by directing WVRs towards satellites, the WVRs themselves could be calibrated.
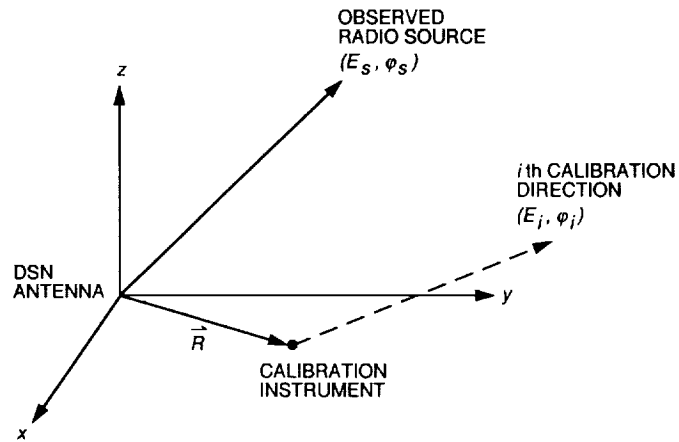
Acknowledgments

Fig. 1. The coordinate system for DSN and calibration directions.
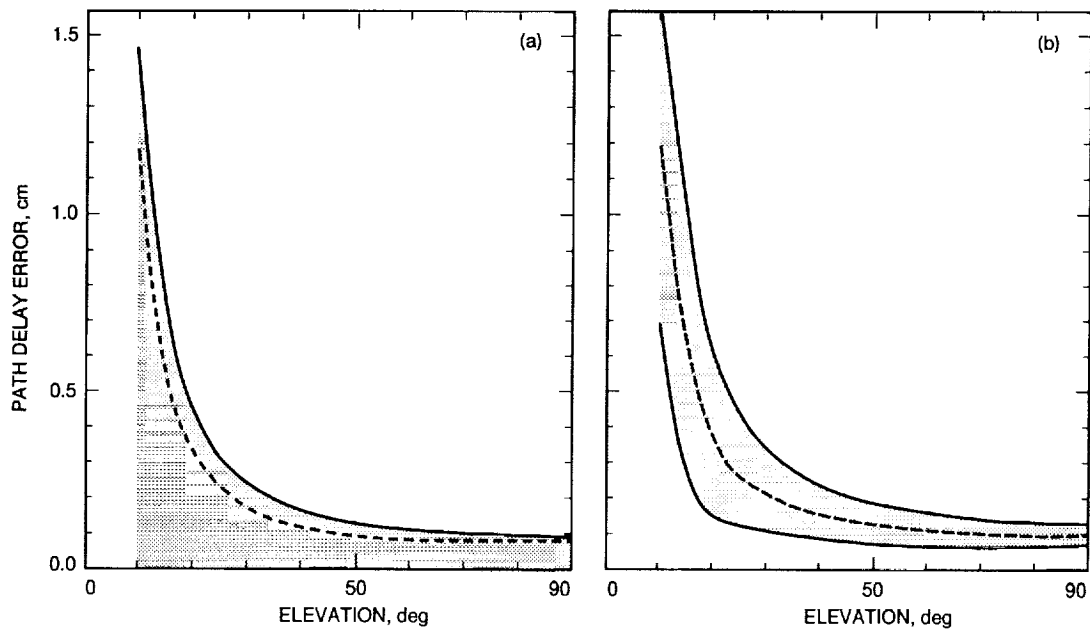

Fig. 2. The instantaneous, tropospheric fluctuation-induced path delay error versus the observed elevation, for (a) R = 0 m and (b) R = 1000 m. The error range is due to the 360-deg range in the observed azimuth, the azimuth of $\vec{R}$, and satellite constellations. The dashed curves are the azimuthally averaged error.
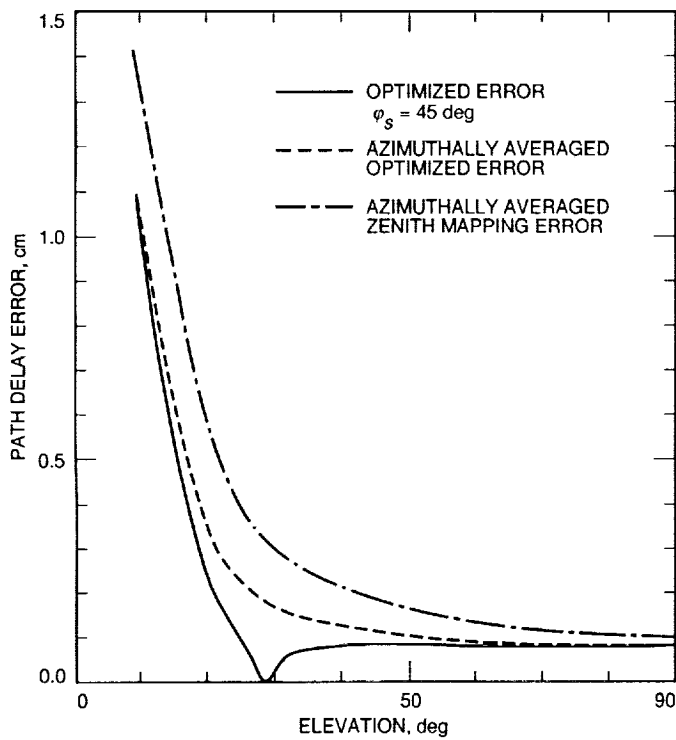
Fig. 3. The tropospheric fluctuation-induced error for one calibration line pointed in the ϕ_l = 45-deg, E_l = 28.4-deg direction ($R = 0$, error-free calibration instrument). The error with optimized c_l's (solid and dashed-line curves) is less than the zenith mapping error (dash–dot curve) by an amount that depends on the elevation.
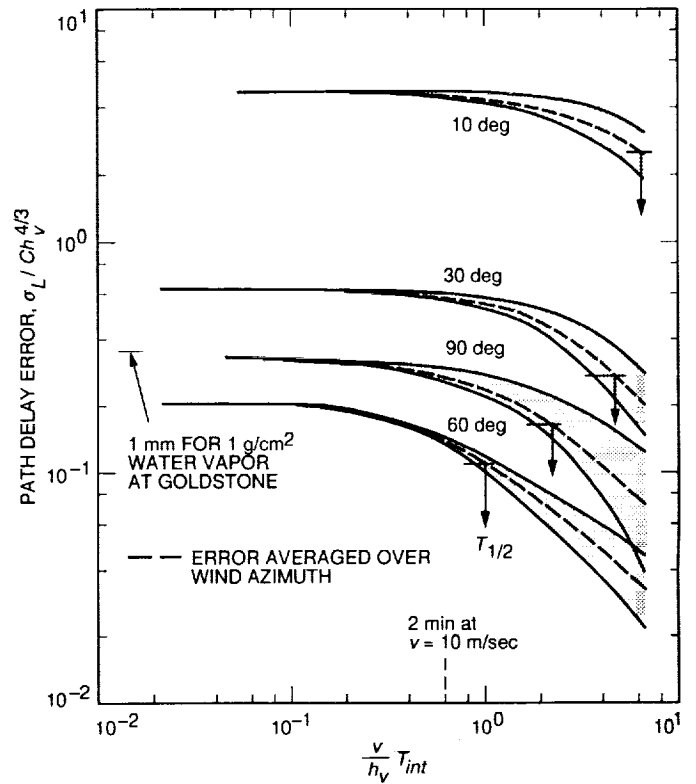
Fig. 4. Tropospheric fluctuation-induced error and the error range (averaged over four principal wind directions) versus the signal integration time T. The azimuth of $\bar{R}$ ($R = 200$ m) is along the azimuth of ϕ_s, $v = 10$ m/sec, and the satellite constellation is for 12:00 a.m., July 1, 1992; C is the turbulence strength constant.
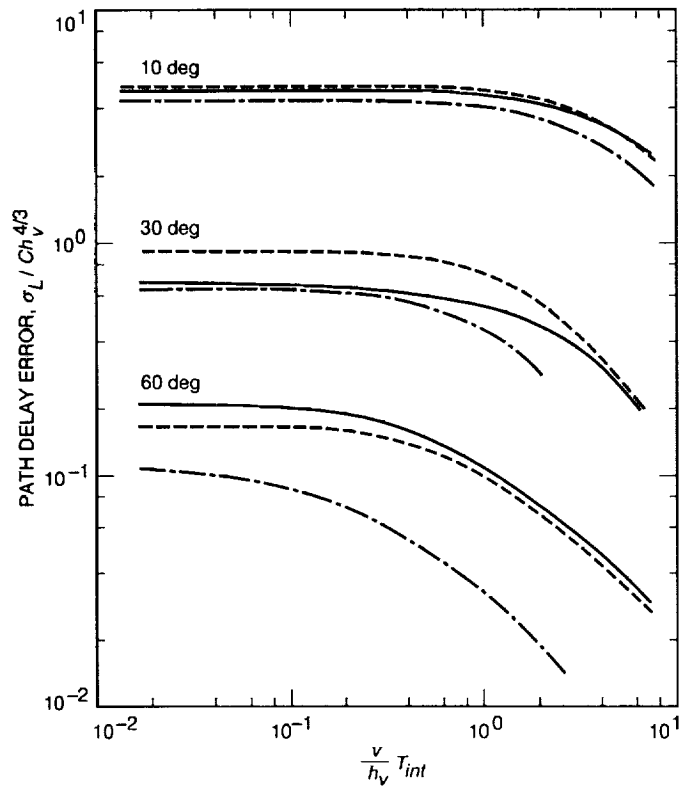
18

Fig. 5. Tropospheric fluctuation-induced error with c_i's optimized for three calibration instruments positioned at corners of an equilateral triangle centered at $R = 200$ m around the DSN antenna (dash–dot line); one instrument located at $R = 0$ (solid line); and one instrument at 200 m (dashed line).
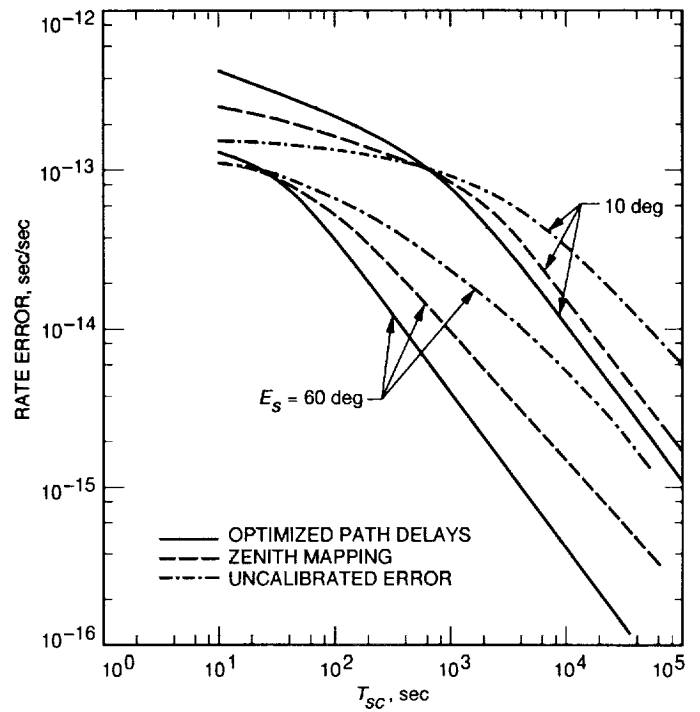
Fig. 6. Tropospheric fluctuation-induced, azimuthally averaged rate error versus scan duration ($R = 200$ m, $v = 10$ m/sec). The error calculated by using the optimized c_i's becomes smaller than the uncalibrated error and the error for zenith mapping at a T_{sc} that depends on elevation.
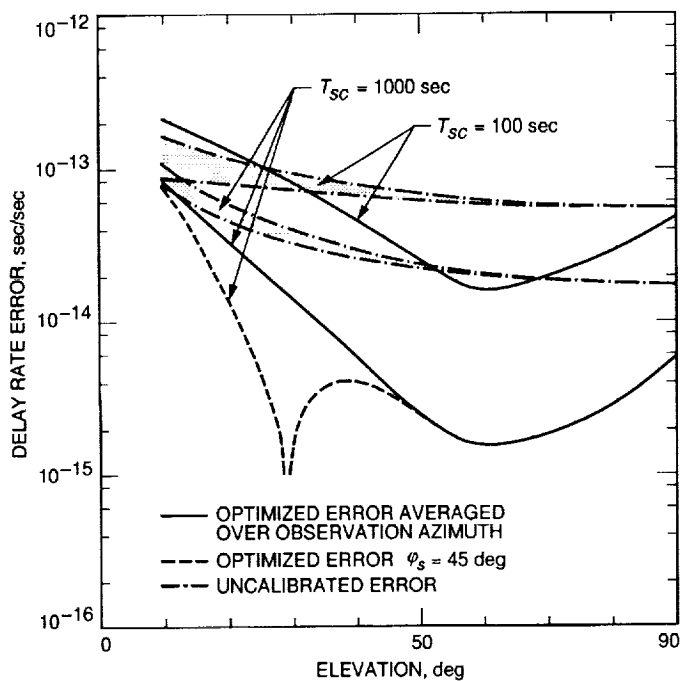
Fig. 7. Tropospheric fluctuation-induced rate error for scan durations T_s = 100 sec and 1000 sec versus E_s when R = 0. The satellite constellation used (12:00 a.m., July 1, 1992) has one satellite in the ϕ_l = 45-deg direction.
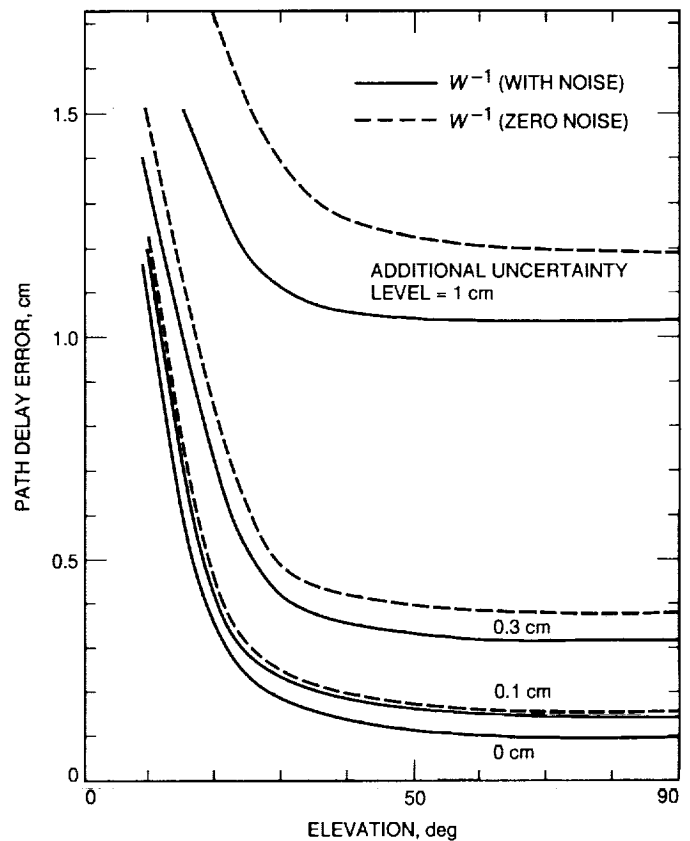

Fig. 8. The combined effect of additional uncorrelated uncertainty levels on the total (azimuthally averaged) error for R = 200 m. The solid-line curves were computed by using c_i's optimized for the additional uncertainty; the dashed lines used c_i's optimized for zero additional uncertainty.

Appendix A

Tropospheric Correlations Using the Kolmogorov Turbulence Model

Path delay correlations are evaluated by writing the path delay at site i and time t as the integral

$$L_{tr,i}(t) = \int_0^{h_v A_i} \chi(\vec{r}_i, t) dr_i \tag{A-1}$$

where the air mass $A_i = 1/\sin E_i$, h_v is the wet troposphere slab height, and $\chi(\vec{r}_i, t)$ is the index of refraction -1 at location $\vec{r}_i$ and time t. For example, the correlation

$$\text{cov}\,(L_{tr,i}(t), L_{tr,j}(t+T)) = (\langle L_{tr,i}(t), L_{tr,j}(t+T) \rangle - \langle L_{tr,i} \rangle \langle L_{tr,j} \rangle) \tag{A-2}$$

is evaluated by substituting Eq. (A-1) and the expression (Eq. (A.3) of [1]):

$$\langle \chi(\vec{r}_i, t) \chi(\vec{r}_j, t+T) \rangle = \langle \chi^2 \rangle - \frac{1}{2} D_\chi(\vec{r}_i - \vec{r}_j + \vec{v}\,T) \tag{A-3}$$

where $\vec{v}$ is the wind velocity, and $D_\chi(\vec{r}_i - \vec{r}_j + \vec{v}\,T) \equiv \left\langle (\chi(\vec{r}_i, t) - \chi(\vec{r}_j, t+T))^2 \right\rangle$ is the structure function for inhomogeneities correlated both spatially and temporally. By interchanging the order of integration and ensemble averaging and setting $dr_i = A_i dz$ and $dr_j = A_j dz'$, Eq. (A-2) becomes

$$\text{cov}\,(L_{tr,i}(t), L_{tr,j}(t+T)) = A_i A_j \int_0^{h_v} dz \int_0^{h_v} dz' \left(\sigma_\chi^2 - \frac{D_\chi(\vec{r}_i - \vec{r}_j + \vec{v}\,T)}{2} \right) \tag{A-4}$$

where the variance $\sigma_\chi^2 \equiv \langle \chi^2 \rangle - \langle \chi \rangle^2$ is independent of spatial coordinates and is obtained by letting the distance R go to infinity in D_χ,

$$\sigma_\chi^2 \equiv \left(\langle \chi^2 \rangle - \langle \chi \rangle^2 \right) = \frac{D_\chi(R = \infty)}{2} \tag{A-5}$$

Assuming that the troposphere is described by the Kolmogorov turbulence model, the structure function for the frozen inhomogeneities is

$$D_\chi(\vec{R} + \vec{v}\,t) \equiv \left\langle \left(\chi(\vec{r}, t) - \chi(\vec{r} + \vec{R} + \vec{v}\,t) \right)^2 \right\rangle = \frac{C^2 |R + \vec{v}\,t|^{2/3}}{1 + (|R + \vec{v}\,t|/L_s)^{2/3}} \tag{A-6}$$

where $\vec{R}$ is the spatial interval over which the structure function is evaluated, the saturation scale length $L_s \simeq 3000$ km, and the turbulence strength $C = 1.1 \times 10^{-7} \text{m}^{-1/3}$ [1,8] (for the wet slab height $h_v \simeq 2$ km, corresponding to about a 6-cm zenith wet path delay at Goldstone).

Equations of the same type were also used to quantify the effect of dry fluctuations. Assuming that the dry fluctuation is one-third of the wet fluctuation [1] with the scale height $h_d \simeq 8$ km, the dry turbulence strength $C_d \simeq (C_v/3)(h_v/h_d)^{4/3} \simeq 9.2 \times 10^{-9}$. For uncorrelated fluctuations, dry and wet errors add in quadrature.

Appendix B

The Delay Rate Error

The delay rate error was evaluated as the square root of the variance of the estimated delay rate, $\hat{B}(T_{sc})$, which is the slope of the path delay over the scan duration T_{sc} [1]. By dividing T_{sc} into N sections of equal length, and assuming that the time origin is in the middle of T_{sc}, a linear fit to points at the centers of the sections gives the following formula:

$$\hat{B}(T_{sc}) = \frac{\sum_i \hat{L}(t_i) t_i}{\sum_i t_i^2} \tag{B-1}$$

where $L(t_i)$ is the delay at the time point t_i at the center of the ith section. By using a similar expression for the actual delay rate, $B(T_{sc})$, the delay rate variance is derived as

$$\sigma_{\hat{B}}^2(T_{sc}) = \left\langle \left(B(T_{sc}) - \hat{B}(T_{sc}) \right)^2 \right\rangle$$

$$= \frac{1}{(\sum_i t_i^2)^2} \sum_i \sum_j t_i \, t_j \, \sigma_{L,tr}^2(t_i - t_j) \tag{B-2}$$

where $i, j = 1, ..., N$, and the path delay variance, $\sigma_{L,tr}^2(t)$, is

$$\sigma_{L,tr}^2(t) = \left\langle \left(L_{tr,s}(t) - \hat{L}_{tr,s}(t) \right) \left(L_{tr,s} - \hat{L}_{tr,s} \right) \right\rangle \tag{B-3}$$

where $L_{tr,s}(t)$, $\hat{L}_{tr,s}(t)$, $L_{tr,s}$, and $\hat{L}_{tr,s}$ are the actual and estimated tropospheric path delays in the observed, (E_s, ϕ_s), direction, at times t and o, respectively.

By using $\hat{L}_{tr,s} = \sum_k c_k L_{tr,k}$ (see the discussion following Eq. (5) of the main text), Eq. (B-2) was evaluated by substituting Eq. (B-3) into Eq. (B-2). This yields

$$\sigma_{\hat{B}}^2(T_{sc}) = \frac{1}{(\sum_i t_i^2)^2} \sum_i \sum_j t_i \, t_j \Big[\text{cov } (L_{tr,s}(t_i - t_j), L_{tr,s})$$

$$+ \sum_k \sum_l c_k c_l \, \text{cov } (L_{tr,k}(t_i - t_j), L_{tr,l})$$

$$- \sum_k c_k \big(\text{cov } (L_{tr,s}(t_i - t_j), L_{tr,k})$$

$$+ \text{cov } (L_{tr,k}(t_i - t_j), L_{tr,s})) \Big] \tag{B-4}$$

where $L_{tr,k}(t)$ are tropospheric path delays in (E_k, ϕ_k) directions at time t. Eq. (B-4) was evaluated for $i = 1, ..., 3$ equally spaced sections within T_{sc} ($t_1 = -T_{sc}/3$, $t_0 = 0$, $t_2 = T_{sc}/3$) by using the Kolmogorov turbulence model described in Appendix A.

References

[1] R. N. Treuhaft and G. E. Lanyi, "The Effect of the Dynamic Wet Troposphere on the Radio Interference Measurements," *Radio Science*, vol. 22, pp. 251–265, March–April 1987.

[2] G. Elgered, J. L. Davis, T. A. Herring, and I. I. Shapiro, "Geodesy by Radio Interferometry: Water Vapor Radiometry for Estimation of Wet Delay," *Journal of Geophysical Research*, vol. 96, no. B4, pp. 6541–6555, April 1991, and references therein.

[3] F. T. Ulaby, R. K. Moore, and A. K. Fung, "Microwave Remote Sensing, Active and Passive," *From Theory to Applications*, vol. 3, Dedham, Massachusetts: Artech House Inc., 1986.

[4] T. Kobayashi, "Techniques for Laser Remote Sensing of the Environment," *Remote Sensing Reviews*, vol. 3, 1987.

[5] W. L. Smith, H. E. Revercomb, H. B. Howell, H.-L. Huang, R. O. Knuteson, E. W. Koenig, D. D. LaPorte, S. Silverman, L. A. Sromovsky, and H. M. Woolf, "GHIS—The GOES High-Resolution Interferometer Sounder," *Journal of Applied Meteorology*, vol. 29, pp. 1189–1204, December 1990.

[6] J. B. Abshire and C. S. Gardner, "Atmospheric Refractivity Corrections in Satellite Laser Ranging," *IEEE Trans. on Geoscience and Remote Sensing*, vol. GE-23, pp. 441–425, July 1985.

[7] W. C. Hamilton, "Statistics in Physical Science," New York: The Ronald Press Company, 1964.

[8] J. Z. Wilcox, "The Effect of Tropospheric Fluctuations on the Accuracy of Water Vapor Radiometry," *The Telecommunications and Data Acquisition Progress Report 42-110, vol. April–June*, Jet Propulsion Laboratory, Pasadena, California, pp. 33–51, August 15, 1992.

[9] D. M. Tralli, S. M. Lichten, and T. A. Herring, "Comparison of Kalman Filter Estimates of Zenith Atmospheric Path Delays Using the Global Positioning System and Very Long Baseline Interferometry," *Radio Science*, vol. 27, no. 6, pp. 999–1007, November–December 1992.